TÜBİTAK

Turkish Journal of Earth Sciences

http://journals.tubitak.gov.tr/earth/

Research Article

Turkish J Earth Sci
(2023) 32: 999-1012

doi:10.55730/1300-0985.1889

# Accuracy assessment of glacier depth monitoring based on UAV-GPR on Horseshoe Island, Antarctica

**Mahmut Oğuz SELBESOĞLU[1], Mustafa Fahri KARABULUT[2,*], Özgün OKTAR[3], Burak AKPINAR[2], Oleg VASSILEV[4], Mehmet ARKALI[1], Şeyma Nur TUFAN[1], Alptuğ Şeref AYYILDIZ[1], Esra GÜNAYDIN[1], Atilla YILMAZ[3], Doğaç Baybars IŞILER[3], Burcu ÖZSOY[3,5]**

[1]Department of Geomatics Engineering, Faculty of Civil Engineering, İstanbul Technical University, İstanbul, Turkiye
[2]Department of Geomatics Engineering, Faculty of Civil Engineering, Yıldız Technical University, İstanbul, Turkiye
[3]Polar Research Institute, TÜBİTAK Marmara Research Center, Kocaeli, Turkiye
[4]Bulgarian Antarctic Institute, Sofia, Bulgaria
[5]Department of Maritime Transportation and Management Engineering, Faculty of Maritime, İstanbul, Turkiye

**Received:** 28.08.2023 • **Accepted/Published Online:** 13.11.2023 • **Final Version:** 28.11.2023

**Abstract:** Unmanned aerial systems have a wide range of uses in studying the impacts of climate change over several fields. Recently, its combination with a ground-penetrating radar (GPR) technology has been demonstrated to be highly effective for surveying glaciers, especially in difficult and inaccessible terrains like Antarctica. In this context, this study focused on exploring the potential of using an unmanned aerial vehicle (UAV)-GPR to measure the depth of glaciers on Horseshoe Island, West Antarctica. The data were collected during the seventh Turkish Antarctic Expedition (TAE-VII) in February and March 2023, within the scope of the international project titled "Glacier monitoring and 3D modeling in Horseshoe Island Antarctica based on UAV-GPR observations", carried out by the bilateral cooperation of İstanbul Technical University and the Bulgarian Academy of Sciences. In order to determine the depth of the glacier, this investigation utilized both terrestrial GPR and UAV-GPR data. The UAV-GPR depth was determined as 9 cm root mean square error as a consequence of comparison with terrestrial GPR results. Furthermore, it was demonstrated that measurements performed with the UAV were completed approximately 25 times faster than those conducted with the terrestrial GPR, demonstrating a significant efficiency benefit. As a result, it can be concluded that using the airborne GPR approach offers a beneficial and effective way to undertake surveys of glaciers quickly and affordably with promising accuracy.

**Key words:** Ground-penetrating radar, Antarctica, Turkish Antarctic Expedition, climate change, glacier

## 1. Introduction

The Antarctic ice sheet offers a unique opportunity to assess the effects of global warming and developing future projections since it plays a crucial role in preserving Earth's climate balance. One of the primary objectives for scientists is to make accurate predictions about the future impact that may occur in the Antarctic continent. These predictions are based on a thorough understanding of the area's natural history, enabling researchers to identify potential risks and develop effective strategies to mitigate them. The presence of glacier regions is one facet of the effects of global warming that is particularly prominent in West Antarctica (Turner et al., 2014). According to the Intergovernmental Panel on Climate Change (IPCC) comprehensive assessment reports on climate change, the continued trajectory of global warming is expected to result in a significant rise in sea level in the near future due to the melting of many glacial zones. Therefore, it is necessary to develop a comprehensive global strategy to address this harmful consequence of climate change. Accurate and high-precision predictions of the future depend on modeling efforts that take into account variables such as the global mean sea level, glacier changes, and alteration rates, making it essential to increase the number of research efforts. From this point of view, various technologies are used to monitor the impact of the climate change caused by global warming on the Antarctic glaciers. These technologies include remote sensing, the Global Navigation Satellite System (GNSS), ground-penetrating radar (GPR), terrestrial, and unmanned aerial vehicle (UAV) photogrammetry (Thompson, 2000; Rignot et al., 2002; Ivins and James, 2005; Rückamp et al., 2011; Selbesoğlu et al., 2023). GPR is a valuable tool in the study of glaciers, especially in remote and harsh

* Correspondence: mfahri@yildiz.edu.tr

environments such as Antarctica (Taurisano et al., 2006; Engel et al., 2012; Campbell et al., 2018). Snow and ice fields, known for their abundant layering and extensive consistency, are ideal locations for exploratory endeavors, making them particularly suitable for the best application of GPR. (Jol, 2008). Furthermore, GPR is used in the field of glaciology, supporting research on various topics such as the examination of diffraction phenomena and the identification of internal stratifications (Engel et al., 2012; F. Benedetto and Tosti, 2017; Forte et al., 2021).

In a study conducted by Healy et al. (2007), GPR was utilized to examine the waterbed topography of Lake Athabasca, which is situated beneath the ice cover. The research aimed to gain a more comprehensive understanding of the lake's subsurface structure, potentially providing valuable insights into the its hydrological and geological processes. The study used two different antennas with center frequencies of 100 and 500 MHz, and measurements were performed by moving the GPR over snow layers of varying thicknesses while attached to an all-terrain vehicle (ATV). As a result of the study, an accuracy of 20 cm in the vertical direction was obtained. Mingo and Flowers (2010) expanded the application of GPR by utilizing a skid unit to measure the thickness of polythermal ice and ice calderas in Iceland and Canada. In Iceland, they used a 10.5-MHz center frequency antenna to detect ice thicknesses up to 550 m. In Canada, a 5-MHz center frequency antenna was employed to study a 220-m glacier. Lamsters et al. (2020) demonstrated the utility of GPR in glacier research by studying the Nye Channel, an ice tunnel in the Russell District of Greenland. They employed a GPR with a center frequency of 38 MHz, manually collecting data to a depth of approximately 160 m. The study was complemented by UAV photogrammetry, which provided additional support for their findings. Precision was obtained as approximately 0.186 m and a standard deviation of 0.043 m in elevation change determined by the GPR. Egli et al. (2021) contributed to the body of knowledge by utilizing the terrestrial GPR method to explore the Haut and d'Ottoma subglacial marginal channels in the Swiss Alps. Employing a GPR with a center frequency of 70 MHz, they carried out measurements with the instrument placed in a backpack, approximately 40 cm above the ground. Additionally, aerial photographs obtained via UAV were used to complement and validate the GPR results. These studies collectively demonstrate the applicability of GPR in various glacial terrains.

Although terrestrial GPR is of better quality overall (Rutishauser et al., 2016), it has some drawbacks, such as difficulties in using it in hard-to-reach areas and the possibility of encountering heterogeneity when used close to the surface.(Merz et al., 2015). Therefore, the airborne GPR approach appears to be a valuable tool for quickly and cost-effectively surveying glaciers and other geological features (Merz et al., 2015). In order to investigate glacier depth, helicopter GPR, which serves the same functions as terrestrial GPR in glacier studies, has been widely employed. Findel and Adler Glacier, Switzerland (Machguth et al., 2006), Indian Himalaya (Negi et al., 2008), Nef and Colonia Glaciers in Patagonia, Southern Chile (Blindow et al., 2012), Furggwanghorn Rock Glacier in Switzerland (Merz et al., 2015), Swiss Alps (Rutishauser et al., 2016), the Rhone Glacier in the Central Swiss Alps (Church et al., 2018), and Glacier de la Plaine Morte in the border region of the Bernese and Valais Alps in SW Switzerland (Grab et al., 2018) are some of the glaciers that have been studied using helicopter GPR.

With recent technological developments, GPR has been used with UAV in hard-to-reach locations. UAV-GPR is employed in security-related situations such as the detection of landmines or improvised explosive devices (IEDs) (Colorado et al., 2017; Fernández et al., 2018; Garcia Fernandez et al., 2020). In inland water bathymetric studies (Bandini et al., 2023a), UAV-GPR has demonstrated a successful performance in detecting the water depth, similar to sonar, which restricts the use of underwater vegetation (Bandini et al., 2023b). Moreover, it has been used in soil moisture estimation and mapping (Wu et al., 2019; Wu and Lambot, 2022a; Cheng et al., 2023), subsurface surveys in mining (Saponaro et al., 2021), buried object detection (Garcia Fernandez et al., 2018), soil electrical conductivity mapping (Wu and Lambot, 2022b), glacier science (Engel et al., 2012; Ruols et al., 2022; Vergnano et al., 2022), and for obtaining snowpack parameters (Jenssen and Jacobsen, 2021).

To summarize, the effectiveness of GPR in studying the complex shape and ever-changing behavior of glaciers in harsh and remote environments such as Antarctica highlights its critical role. When the existing studies were examined, it was seen that very limited research has been conducted to determine glacier depth using UAV-GPR. For this purpose, the current study focused on investigating the potential of using UAV-GPR to obtain depth information of glaciers on Horseshoe Island, West Antarctica, through the data set obtained during the seventh Turkish Antarctic Expedition (TAE-VII) in February and March 2023. These results can also serve as a valuable reference for future research on the use of UAV-GPR to determine glacier depth in harsh and hard-to-reach environments.

## 2. Materials and methods

### 2.1. GPR

GPR is a nondestructive testing technique that comprises a radar control unit, data storage, and display devices, along with transmitting and receiving antennas, and this

technique is used in many geoscience studies such as soil, bedrock, groundwater, and ice detection (Jol, 2008).

GPR operates on the fundamental principle of recording the time duration it takes for electromagnetic waves to travel from the transmitting antenna to the underground target and reflect back to the receiving antenna. It has been observed that when GPR signals encounter interfaces with varying dielectric coefficients, they tend to spread, while the reflected signals are efficiently collected by the receiving antenna (Benedetto and Tosti, 2017) (Figure 1).

The basis of the GPR system based on the electromagnetic (EM) wave theory and the physics of EM fields have been mathematically defined by Maxwell's equations. The quantitative foundation of the GPR signal is established by determining the material properties with structural relations and combining the information.

These Maxwell's equations are depicted in Eqs. (1)–(4) below (Jol, 2008):

$$\nabla^{-} \times E^{-} = -(\partial B^{-}) / (\partial t), \quad (1)$$

$$\nabla^{-} \times H^{-} = J^{-} + (\partial D^{-}) / (\partial t), \quad (2)$$

$$\nabla^{-} \cdot D^{-} = q, \quad (3)$$

$$\nabla^{-} \cdot B^{-} = 0, \quad (4)$$

where $E^{-}$ is the electric field strength vector (V/m), $H^{-}$ is the magnetic field intensity (A/m), $B^{-}$ is the magnetic flux density vector, $J^{-}$ is the electric current density vector (A/m$^2$), $D^{-}$ is the electric displacement vector (C/m$^2$), q is the electric charge density (C/m), and t is the time.

Based on these relationships, it can be said that all classical EM phenomena (induction, radio waves, resistivity, circuit theory, etc.) can be derived from the electrical properties of the material. Constitutive relationships are the material's response to the EM fields. For GPR studies, the electrical and magnetic properties are consequential, as shown in Eqs. (5)–(7) below:

$$J^{-} = \sigma^{\sim} E^{-}, \quad (5)$$

$$D^{-} = \varepsilon^{\sim} E^{-}, \quad (6)$$

$$B^{-} = \mu^{\sim} H^{-}. \quad (7)$$

Here, $\sigma^{\sim}$ represents the free charge movement in the electric field, while $\tilde{\mu}$ describes how the intrinsic magnetic moments respond to the magnetic field.

GPR traces are the result of reflected signals and are presented in radargrams (Figure 2) that include velocity data, thereby providing crucial information on underground depths.

The point to be noted here is that the data on the Y-axis of the graph can be depth, time, samples, and altitude information. In addition, there are trace numbers on the X axis. When viewing the data collected within the scope of the project in a digital environment, the resulting image may be challenging to interpret. To address this issue, necessary data processing steps (refer to Section 2.2) were applied to the raw data with the aim of obtaining a more easily interpretable image. Furthermore, filtering techniques were employed to enhance the signal-to-noise raito (SNR) across the entire dataset.

### 2.2. Filtering steps

A radargram serves as a visual representation of the reflections of underground electromagnetic waves. To enhance operational efficiency and minimize unwanted signals, commonly referred to as noise, data processing is employed. In the scope of this study, a series of data processing steps were applied, including time zero correction, background removal, deconvolution, and low-pass filter. Time zero correction is used to detect the time spent by the signal traveling between the transmitting and receiving antennas (Steinbeck et al., 2022). The straight lines observed in the background of the image are

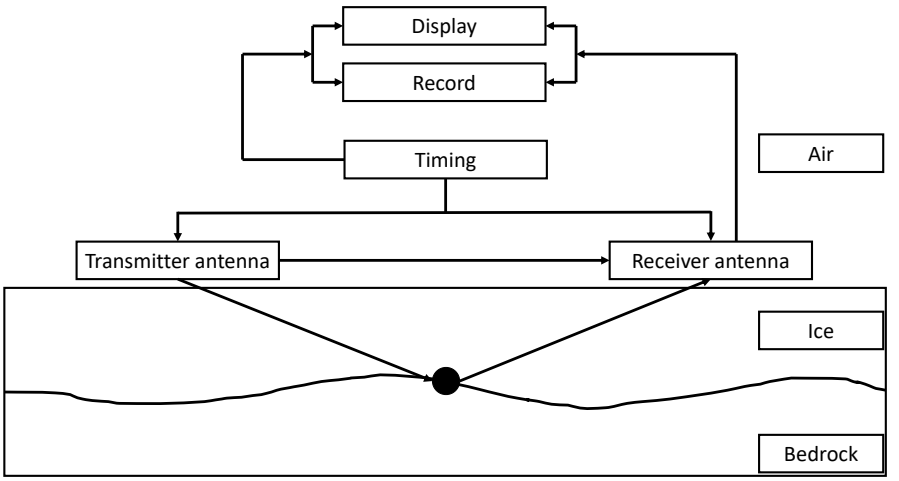


**Figure 1.** Working principle of the GPR (Jol, 2008).

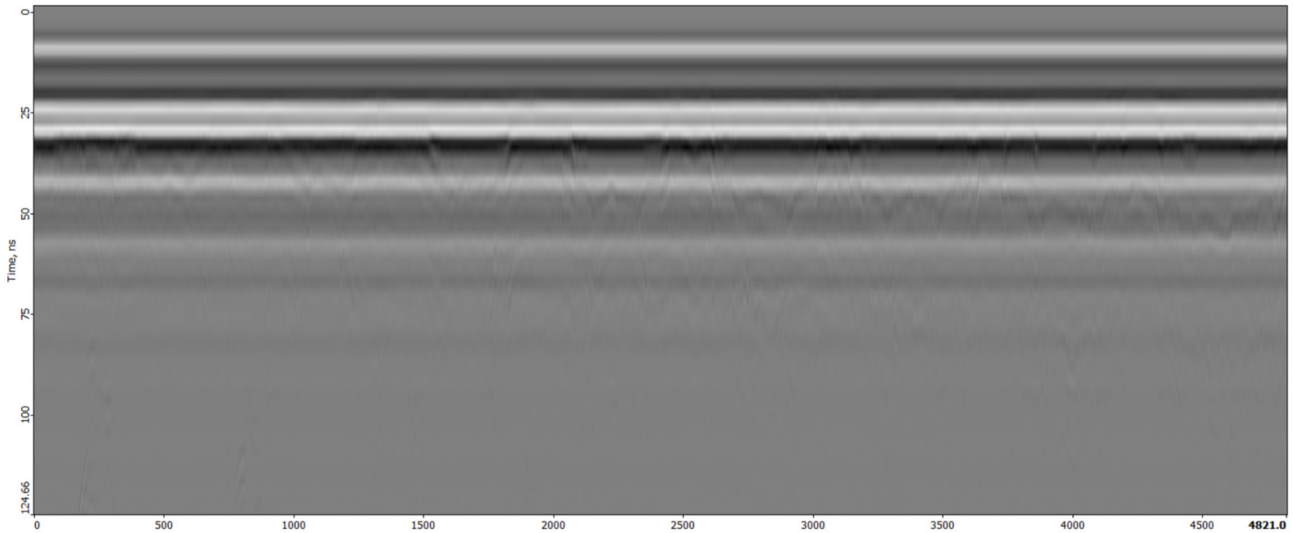


**Figure 2.** Raw radargram image.

referred to as ringing. The ringing effect, can be caused by the interaction of antennas and electrical cables, cell phones, etc. (Bianchini Ciampoli et al., 2019). When these effects are removed from the image with the background removal filter, the image becomes highly interpretable. The deconvolution filter, which has rarely been applied in the literature, enhances temporal resolution for clearer visualization of the region of interest on the radargram (Economou et al., 2015). Horizontal low-pass filtering eliminates low-frequency noises generated by other objects (e.g., vehicles, buildings, trees) (Benedetto et al., 2017). Moreover, the low-pass filter creates a smoothing effect on the radargram image.

### 2.3. Error analysis of the retrieval glacier depth

There are two important factors that can significantly affect the accuracy of the glacier depth measurements. First, the chosen transmission velocity may contain potential errors that are utilized to convert time to depth. Second, a timing error could take place when identifying the epoch of measurement, particularly the moment when the bed reflection appears within the recording. In order to achieve high accuracy in the results, it is imperative to consider these factors when analyzing and assessing ice thickness measurements.

The ice thickness can be calculated as shown in Eq. (8):

$$H = \frac{v \times t}{2}. \quad (8)$$

Here, v is the sound velocity (transmission velocity) in the medium (ice is equal to 168 m $\mu s^{-1}$) and t is the normal moveout (NMO) corrected two-way travel time (TWTT).

The NMO adjustment will normally only have an impact on the shallowest regions of the profiles since the profiling offset (distance between antenna centers) is typically considerably lower than the ice thickness. Thus, according to Dix (1955) and Yilmaz (2001), the adoption of a flat reflector NMO correction should be enough, as given in Eq. (9):

$$t = \sqrt{t_r^2 - \left(\frac{d}{v}\right)^2}. \quad (9)$$

According to Navarro et al. (2014), the errors in the transmission velocity and in t can be considered independent. As a result, when error propagation is applied to Eq. (10), as done by Bevington et al. (1993), we obtain:

$$\sigma_{HGPR} = \frac{1}{2}\sqrt{t^2\sigma_v^2 + v^2\sigma_t^2} \quad (10)$$

Here, σ denotes the error of the variables.

According to Lapazaran et al. (2016b), the uncertainties of RWV ($\sigma_v$) lie between ~1 and 5% of the transmission velocity in the medium (±1.7 to ±8.4 m $\mu s^{-1}$) and uncertainties of t ($\sigma_t$) equal to 1/f (f is the center frequency of the GPR device). Accordingly, for example, the accuracy of a 200-ns TWTT measurement performed with a 120 MHz center frequency device is determined as 0.72 m (approximately 5% of the depth value). The uncertainties of the depths range between 2% and 15% of the ice depth (Godio and Rege, 2015; Fu et al., 2018; Richards et al., 2023).

### 2.4. Interpolation methods

A comprehensive analysis was conducted to assess the accuracy of a digital depth model. Various interpolation techniques such as inverse distance weighting (IDW), Kriging, natural neighbor interpolation, and polynomial regression were employed in the study. The results obtained

from the analysis were used to determine the effectiveness of the digital depth model.

The IDW interpolation method determines cell values by linearly weighting the location-dependent variable points with the inverse distance function. The effect of the weighting decreases as the points forming the surface move away from the sampled location (Rippa, 1999; Mueller et al., 2004), as shown in Eq. (11):

$$Z_0 = \frac{\sum_{i=1}^{N} z_i \cdot d_i^{-n}}{\sum_{i=1}^{N} d_i^{-n}}. \quad (11)$$

Here, $Z_0$ is the value of variable z at point I, $z_i$ is the value of sample at point I, $d_i$ is the distance between the sample and estimated point, N is the coefficient of weight based on a distance, and n is the total number of predictions.

The primary factor affecting the accuracy of the resulting surface is the value of the power parameter, denoted as P, used in the IDW method. The P parameter allows for determining the contribution of the sampled points with respect to the inverse of the distance of the points used to generate the surface. In other words, the P parameter determines the impact of each point on the formation of the surface.

The Kriging interpolation method involves generating a variance surface by applying mathematical operations to a given number of data points or points within a specific radius. This method is based on the assumption of spatial correlations between points in terms of their distances and directions. The Kriging method consists of three distinct steps: statistical data analysis, variogram modeling, and the creation of a variance surface. This approach is particularly suitable for situations where the distance and direction deviation of the data are known, as outlined by Lam (1983) in Eq. (12):

$$\hat{Z}(s_0) = \sum_{i=1}^{N} \lambda_i Z(s_i). \quad (12)$$

Here, $Z(s_i)$ is the value obtained by measuring at the *i*th location, $\lambda_i$ is the measured value at the *i*th location has an unknown weight, $s_0$ is the predicted location, and N is the total number of measured values.

The natural neighbor interpolation method, developed by Sibson (1981), utilizes Voronoi diagrams to extrapolate spatial data from a given sample dataset. Commonly referred to as the Sibson or area-staling method, it ensures that the resulting surface heights lie within the range of the original dataset. This approach is a valuable tool for professionals seeking to interpolate spatial data accurately and efficiently. The algorithm's input data consists of a set of points $\{(x_i, y_i)\}_{i=0}^{N}$ each associated with corresponding function values specified as. $f\{(x_i, y_i)\}_{i=0}^{N}$. The algorithm relies on computing Voronoi diagrams for the initial points $(x_i, y_i)$ and producing a tessellation by recalculating the interpolated locations (x, y). How much of the area of the initial diagram elements was stolen by the region of the newly inserted point depends on the value G(x, y), which is assigned to the interpolated point, as given below in Eq. (13):

$$G(x, y) = \sum_{i=1}^{N} w_i f(x_i, y_i). \quad (13)$$

The measured value at position $(x_i, y_i)$ is represented by the symbol *f*, and $w_i = \frac{Q_k}{R_k}$ is a proportion of the stolen area. The initial Voronoi diagram element for point $P_k$ is represented by $R_k$, and the newly created element for point (x, y) is represented by $Q_k$, which is the area where $R_k$ and $Q_k$ intersect (Sibson, 1981).

The methodology employed in this data analysis involved the utilization of polynomial regression, which helps uncover underlying patterns and trends. While polynomial regression is an effective tool for trend surface analysis, it is important to note that subtle nuances within the data may be obscured. Furthermore, this technique has the ability to extrapolate grid values beyond the range of available data, thereby predicting the value of an independent variable in terms of the predicted value of the dependent variable. The model in basic linear regression is seen below in Eq. (14):

$$Z(x,y) = A + Bx + Cy. \quad (14)$$

Here, Z is the dependent values, and x and y are the predictors. Consequently, each of the two predictor variables is regressed on the outcome variable. A, B, and C are the coefficients of the polynomial regression least square estimation (Shanock et al., 2010).

### 2.5. Terrestrial GPR and UAV-GPR comparison

In order to compare the depths obtained from the terrestrial GPR and UAV-GPR methods, both data sets were analyzed using the filtering techniques mentioned in Section 2.2. After this process, the depth values were obtained by digitizing the radargrams. The data obtained from the terrestrial GPR measurement were accepted as true values and the surface was created using the local polynomial method to compare it with the UAV-GPR depths. The depth values obtained by the UAV-GPR from this surface were compared and the differences were calculated. The root mean square error (RMSE) of the UAV-GPR depths was calculated using the formula below in Eq. (15):

$$\mathrm{RMSE} = \sqrt{\frac{1}{n}\sum_{i}^{n}(dt - du)^2}. \quad (15)$$

Here, dt represents the depth obtained from the terrestrial GPR measurements, while du represents the

depth obtained from the UAV-GPR, and n represents the number of data.

Data beyond the range of ±3 RMSE from the mean of the difference values were considered as gross error and excluded from the data set. The RMSE value of the data set was recalculated using Eq. (15) and the accuracy of the data obtained with the UAV-GPR was determined.

**2.6. Study area**

The study focused on Horseshoe Island, located in the west of the Antarctic Peninsula and known as the third largest island in the Marguerite Bay archipelago, where the Turkish base is located. The total area of Horseshoe Island is 60 km$^2$, and 66% of the island is made up of glaciers or semiperennial ice and snow. As a result of meteorological measurements at the Rothera (1977–2015) and San Martin (1985–2015) stations, which are close to Horseshoe Island, it was observed that the annual average air temperatures are –4.3 and –4.6 °C, respectively (Oliva et al., 2017).

The chosen study area, where the measurements were conducted with GPR, was close to the area where the Turkish temporary base is located (Figure 3). In addition, the determination of glacier changes is one of these reasons why it is the basis for studies to be carried out to determine the possible areas of a scientific base to be established in the future. Another is that, as can be seen in Figure 3, on the southwest side of the area, the glaciers end, and the terrain begins. It will be easier to verify the results obtained from the GPR measurements performed in this

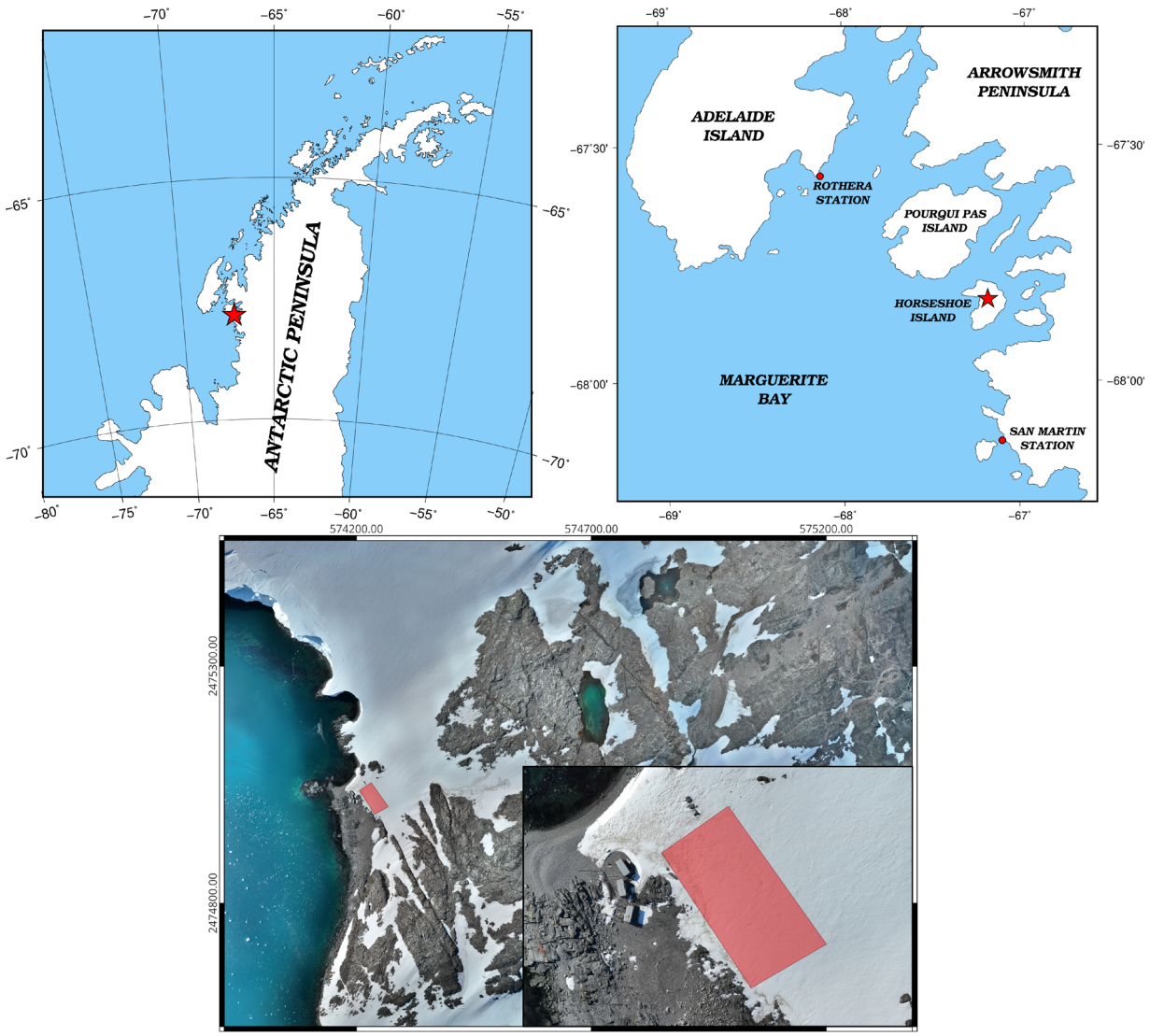


**Figure 3.** Image of the study area.

section. So much so that in this part, the ice depth can be determined manually using primitive tools to determine the glacier depth. Moreover, it was decided to be close to the base area in order to use the limited time efficiently during the expedition.

The study area to be measured, which was approximately 2500 m², was scanned in 21 lines using a wheeled cart and 17 lines using a UAV, as shown in Figure 4. The average distance between the lines measured with the terrestrial GPR and UAV-GPR was approximately 2 m. With the GPR (the same device used in the terrestrial measurements) mounted on the UAV, measurements were carried out from a height of approximately 3 m, following the terrain.

Raw data were gathered as a result of the measurements carried out in the field. During the measurements, ice was selected as the material type parameter in order to generate the depth information of the study area and to obtain the horizontal positioning of the GNSS receiver, both the terrestrial and UAV-based methods were used.

Figure 5 demonstrates the lines obtained as a result of the measurements. A total of 21 lines of data, each approximately 40 m in length, were collected with terrestrial GPR. The distance between each trace, that is, between the 2 depth data on the lines, was around 10 cm. Accordingly, there were approximately 400 traces in each line. A total distance of 850 m was covered to collect these data, and the measurement was completed in approximately 2–3 h.

In the measurement made with the UAV-GPR, a total of 17 lines of data were obtained, each approximately 60 m in length. The distance between each trace, that is, the distance between the 2 depth data points on the lines, was around 20 cm. Accordingly, there were approximately 300 traces in each line. Considering that the flight speed was set at 2 m/s, the measurement was completed in approximately 9 min.

In addition, analysis was performed by decimating the lines in order to determine the surface accuracy of the data obtained from the terrestrial GPR measurements. In 2 different scenarios, different interpolation methods were performed by taking 4 m between the lines first and 8 m between the lines in the other scenario. Lines not used in the surface interpolation were used as test data. Figure 6 shows the model and test data used in the 2 different scenarios.

## 3. Results

In order to get the depth information from raw radargram data several data processing steps were applied, such as background removal, horizontal low-pass filtering, and zero-time correction. The image shown in Figure 7 displays the resultant product obtained from the data processing of a line in the southern part (Figure 6). In this way, the radargram image formed as a result of each processing step and the red digitization (manually digitized) line on the last radargram was obtained.

As stated above, the uncertainty value of the depths obtained in Section 2.3 varied between about 2% and 15% of the depth. The uncertainty of the depths obtained by taking this approach into account varied between 0.02 and 0.14 m. The average of these values was determined as 0.08 m.

In order to determine the accuracy of the surface to be obtained from these values, the depth uncertainty ($\sigma_{HGPR}$) and interpolation uncertainty ($\sigma_{HINT}$) values obtained for each point were used (Lapazaran et al., 2016a):

$$\sigma_{H} = \sqrt{\sigma_{HGPR}^2 + \sigma_{HINT}^2}. \quad (15)$$

**Figure 4.** GPR measurements.

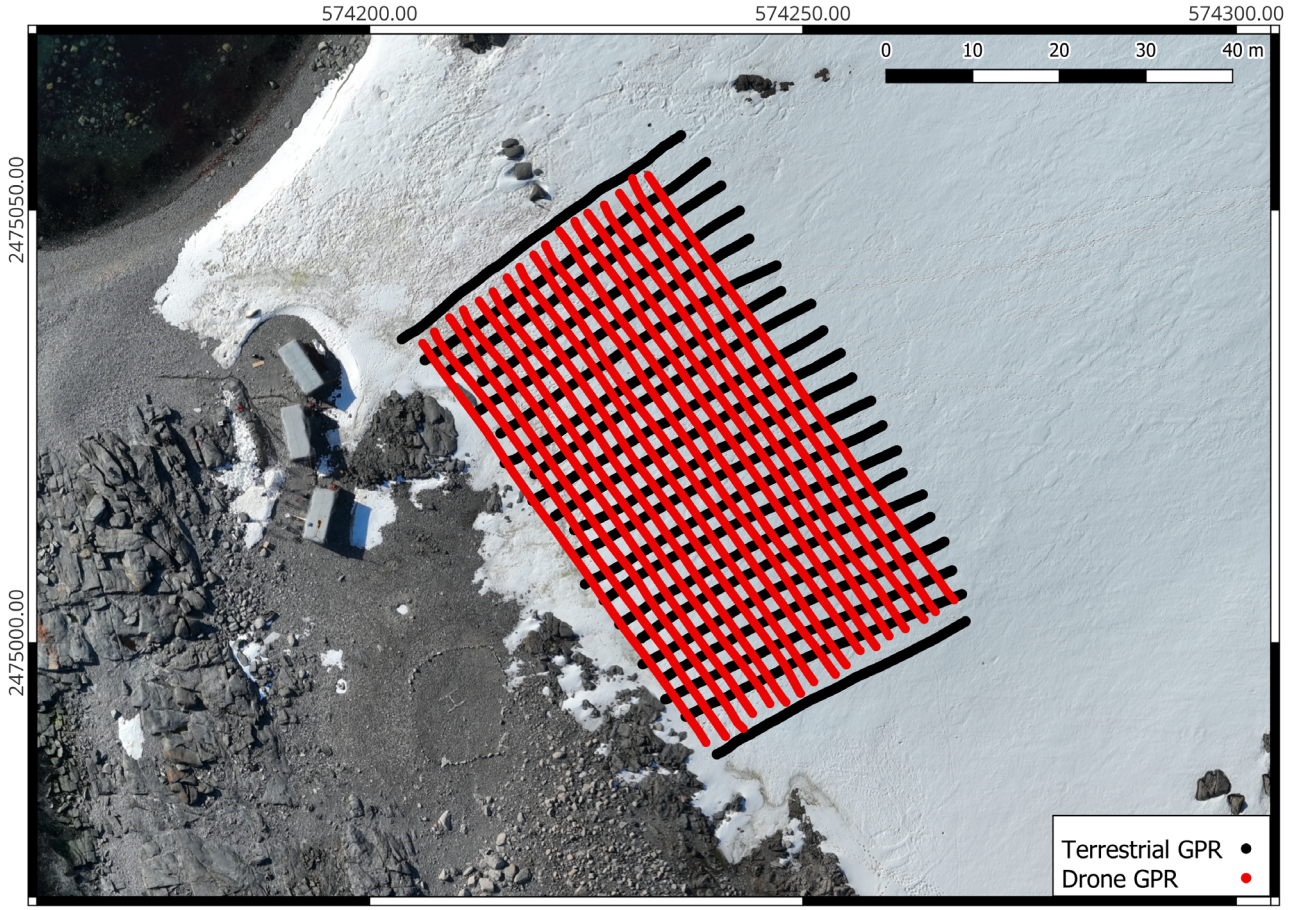


**Figure 5.** GPR measurement lines (black lines are terrestrial GPR and red lines are UAV-GPR measurements).

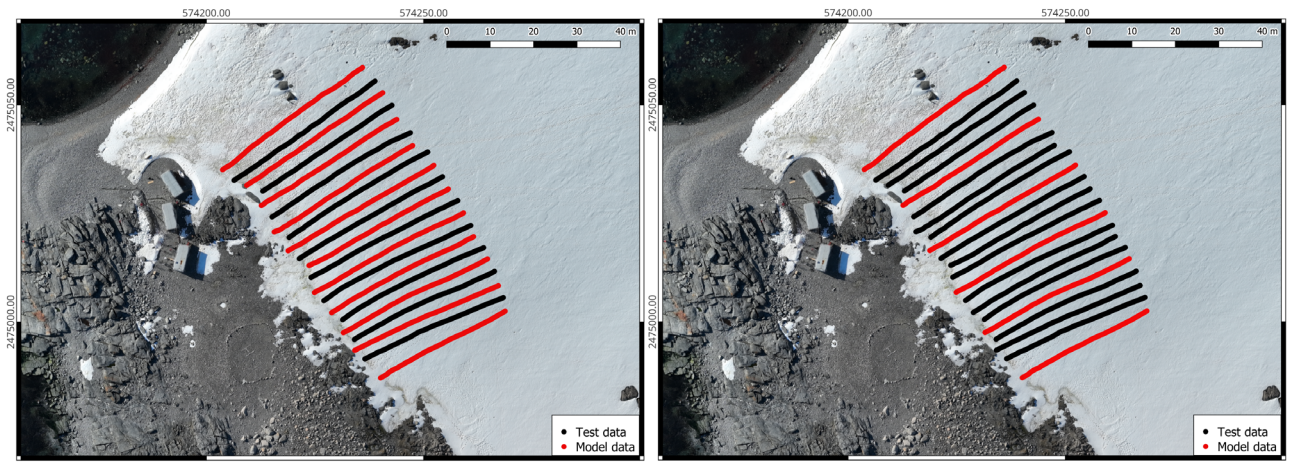


**Figure 6.** Terrestrial GPR lines, left side is scenario 1 and the other is scenario 2 (black lines are test and red lines are surface model data).

If Eq. (15) is applied to each point, the error map of the model can be obtained. However, to estimate the ice-volume error, evaluate the overall quality of the digital elevation models, or compare their accuracy, it may be helpful to define the overall quality of the ice-thickness depth model using a single parameter. The RMS value

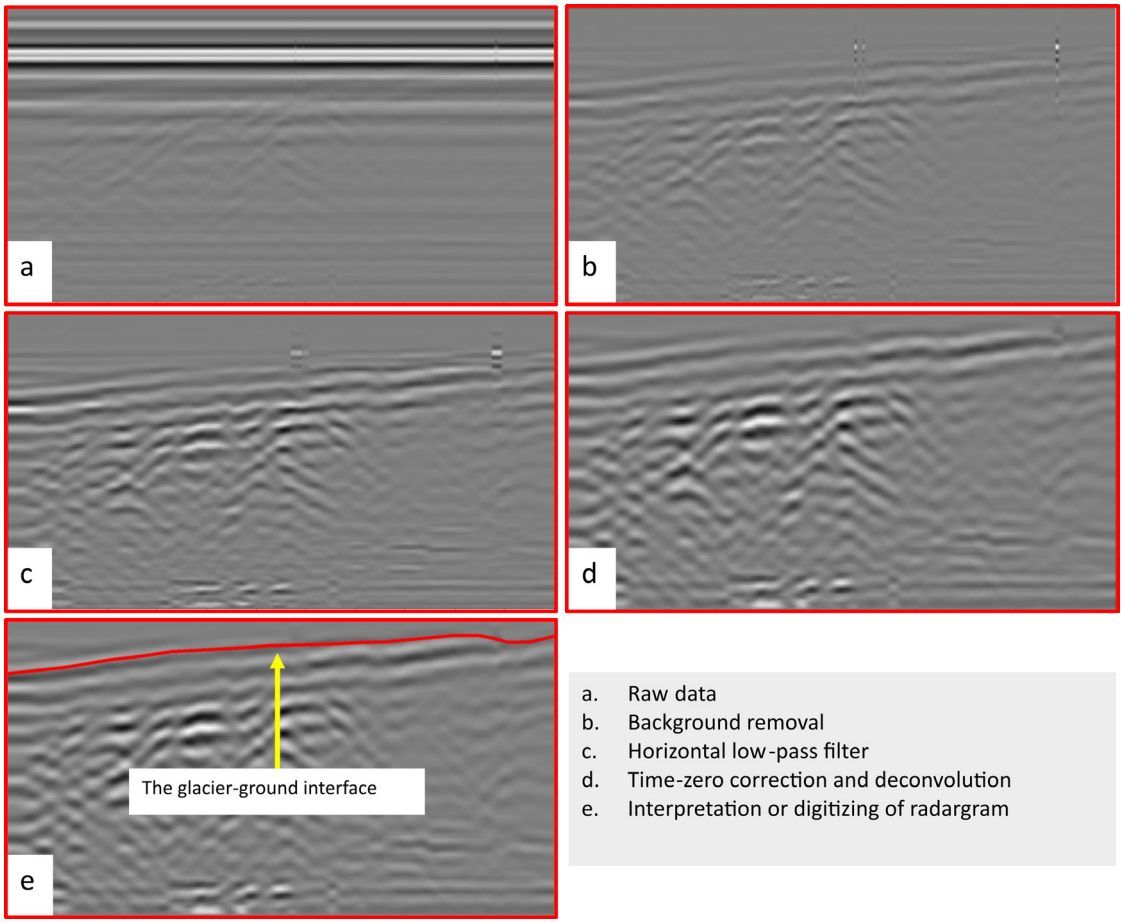


**Figure 7.** Processing steps for the GPR data (the southernmost line of the map in Figure 6).

of the errors at all of the grid nodes can be used in these situations, using Eq. (16) below:

$$\sigma_{\text{HDepthModel}} = \sqrt{\frac{1}{N}\sum_{k=1}^{N}\sigma_{\text{H}}^{2}}. \quad (16)$$

Here, N is the node number.

In order to determine the accuracy of the interpolation, the lines shown in red in the data given in Figure 6 were used as input to the model, and the lines shown in black were compared. This process was carried out in 2 different scenarios. In scenario 1, the distance between the lines was approximately 4 m, and in scenario 2, the distance between the lines that were input to the model was 8 m. That is, the power and smoothing values for the IDW were entered as 2 and 0, respectively. Kriging was chosen as linear, the slope value was taken as 1, the kriging type was chosen as a point, and the drift type was selected as none. The ratio and angle, which are the anisotropy values of the IDW, kriging, and natural neighbor methods, were entered as 1 and 0, respectively. In the polynomial regression method, the simple planar surface was selected, and the maximum x, y, and total orders were entered as 1.

RMSE values were calculated by taking the residuals between the data obtained as a result of the modeling and the test data. The minimum, maximum, average, and RMSE values of these residual values are given in the Table for each method and scenario.

Accordingly, it was seen that the best result was the local polynomial method, with an interpolation accuracy of 0.09 cm with lines at 4-m intervals, and 0.11 cm with interpolation at 4-m intervals. As a result, the interpolation accuracy of each point averaged 0.10 m. When the 0.08-m depth and 0.10-m interpolation accuracy values obtained were put in their places in Eq. (15), the uncertainty of each point was obtained as 0.13 m. Since this value was assumed to be the same for every point in the area, this value can be directly expressed as the accuracy of the model obtained.

As mentioned in Section 2.5, the difference values were calculated by comparing the surface obtained by the local polynomial method using the terrestrial GPR data and the UAV-GPR results.

As can be seen in Figure 8, the mean of the differences was approximately 2.9 cm and the RMSE value was 9.3 cm. It is seen that the difference values were in accordance with the normal distribution. Values outside of the 99.7% confidence interval were excluded from the data set, and as a result of recalculation, the mean value was 2.8 cm and the RMSE value was 8.9 cm (Figure 9).

The map obtained by removing the coarse incorrect values from the data set is shown in Figure 10.

Figure 10, it can be seen that large differences occurred in the boundary of the model. The reason for this can be stated that the interpolation method did not work well outside of the model.

**Table.** Result of different interpolation methods.

| | **Scenario 1** | | | | **Scenario 2** | | | |
|---|---|---|---|---|---|---|---|---|
| | Min | Max | Mean | RMS | Min | Max | Mean | RMS |
| | (cm) | | | | (cm) | | | |
| IDW | –0.16 | 0.31 | 0.06 | 0.12 | –0.26 | 0.40 | 0.05 | 0.14 |
| Kriging | –0.16 | 0.35 | 0.06 | 0.12 | –0.24 | 0.31 | 0.05 | 0.12 |
| Natural neighbor | –0.18 | 0.32 | 0.06 | 0.12 | –0.25 | 0.29 | 0.05 | 0.12 |
| Local polynomial | –0.18 | 0.25 | 0.03 | 0.09 | –0.23 | 0.27 | 0.03 | 0.11 |

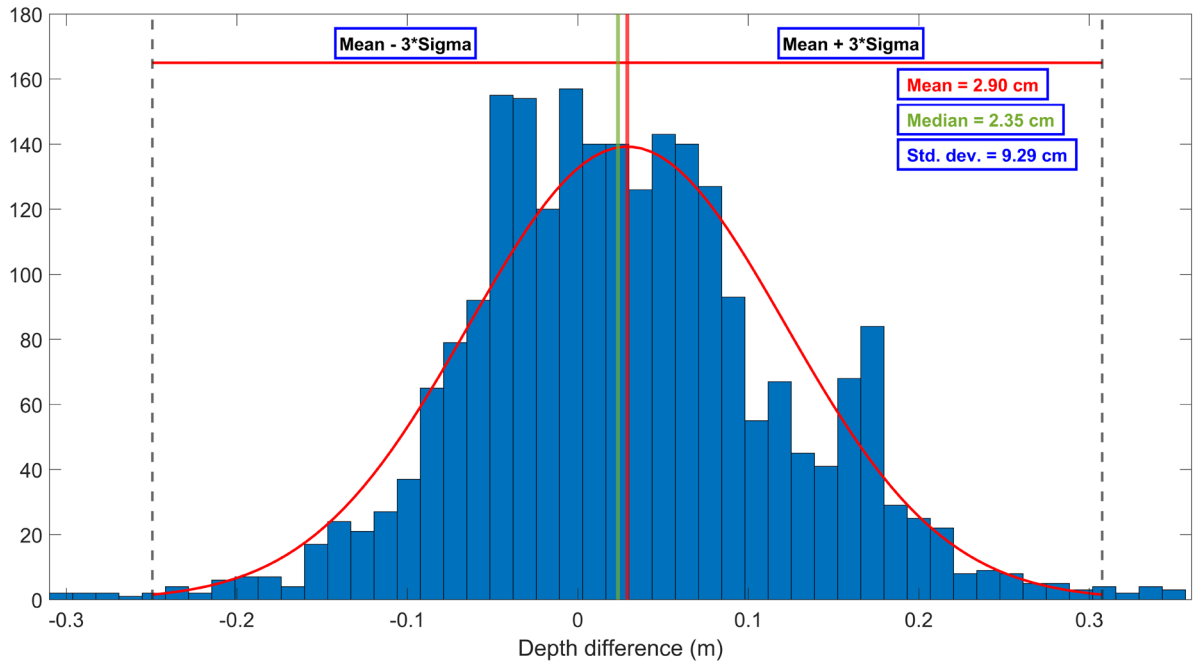


**Figure 8.** Distribution graph of the differences between the terrestrial GPR and UAV-GPR.

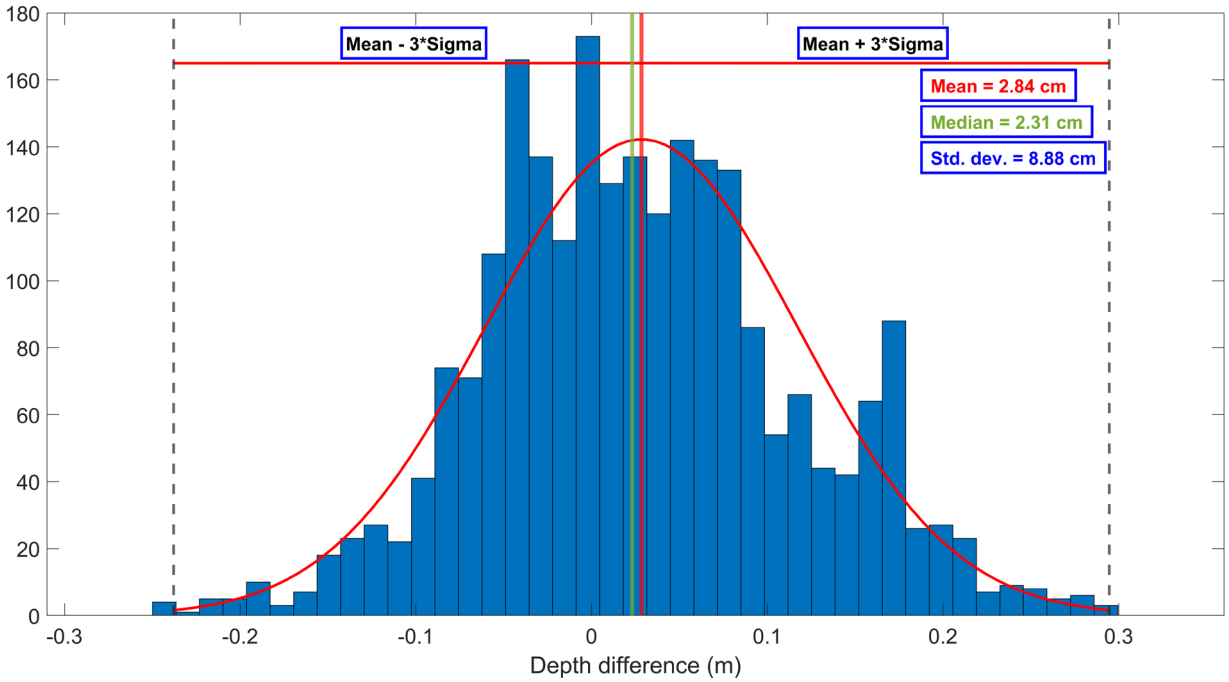


**Figure 9.** Distribution graph of the differences between the terrestrial GPR and UAV-GPR.

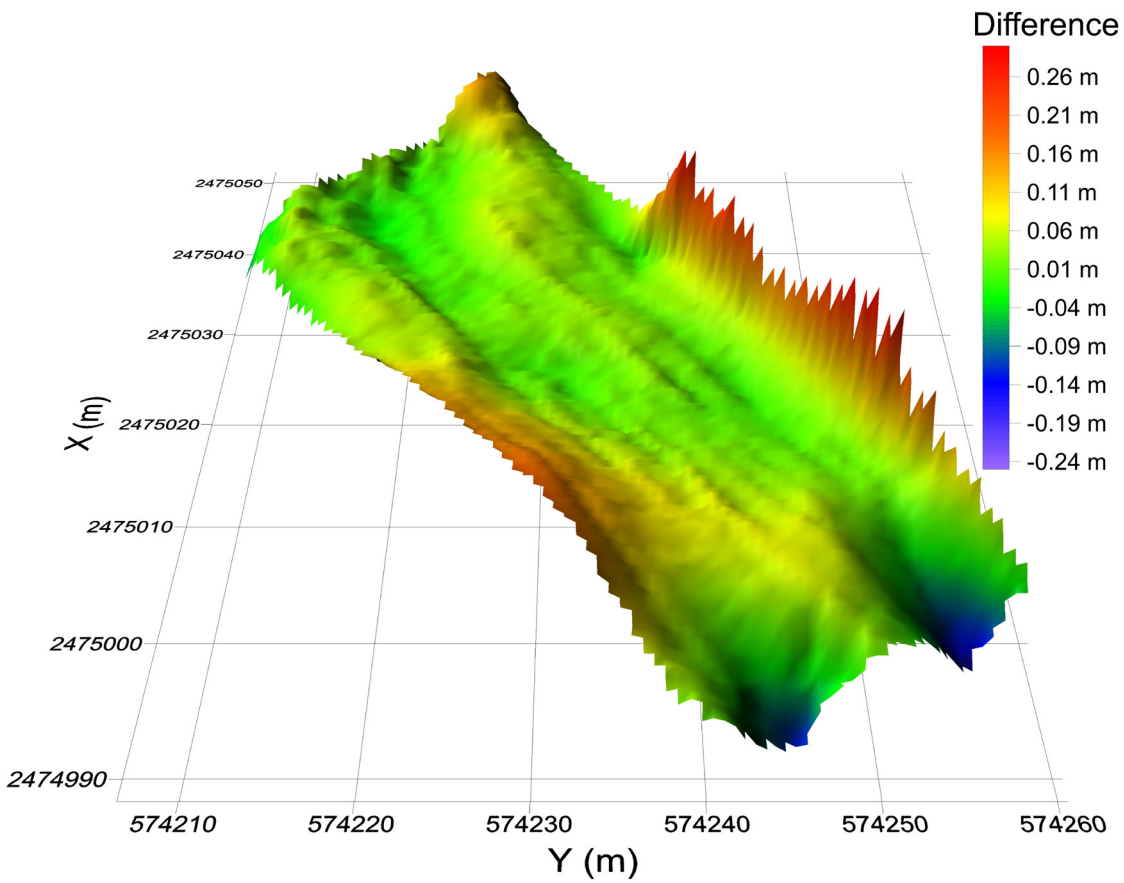


**Figure 10.** Difference value visualization.

## 4. Discussion

In the study, the depth of the glacier was determined by terrestrial GPR and UAV-GPR data through TWTT, which can be influenced by environmental factors such as temperature, water content, and the presence of a cavity structure. Additionally, the accuracy of glacier depth determination is affected by the variability in the terrain height. However, the study area had an almost homogeneous structure. The literature indicates that depth determination accuracy is directly proportional to increasing depth (Engel et al., 2012; Ai et al., 2014; Navarro et al., 2014; Lapazaran et al., 2016a). In the current study, the accuracy of the depth determination of the glacier was found to be comptatible with the literature. When the interpolation methods revealed in terms of accuracy with data attenuated at 4- and 8-m intervals, the results were found quite close to each other. However, the local polynomial method was one step ahead of the others. The fact that these values were close to each other showed that the interpretation of the radargram, which greatly affects the accuracy of the depth information obtained and requires experience, was performed correctly. The depth determination based on the GPR and interpolation methods was investigated in terms of accuracy through the terrestrial GPR depth uncertainty ($\sigma_{HGPR}$) and interpolation uncertainty ($\sigma_{HINT}$) values obtained for each point. According to Eq. (15), the glacier depths were determined with a RMSE of approximately 13 cm from the local polynomial surface model.

In addition, the accuracy of the UAV-GPR measurements was investigated. As a result of these evaluations, the values obtained from the UAV-GPR were compared with those of the terrestrial GPR and the average of the differences was calculated as 0.03 m with a RMSE of 0.09 m. Measurements performed with the UAV were completed approximately 25 times faster than the terrestrial GPR. Accordingly, the UAV-GPR can scan 25 times more per unit time and its accuracy is around 0.09 m compared to the terrestrial GPR.

## 5. Conclusion

The study demonstrates that the integration of GPR technology with UAVs offers an efficient approach for mapping glaciers in challenging environments. Furthermore, the results indicated that GPR-UAVs are an important tool for glaciological research and environmental monitoring that can rapidly conduct surveys of glaciers with a promising degree of accuracy. The UAV-GPR is a flexible tool with a wide range of applications because it can carry out quick surveys, even in challenging environments. In future stages of this study, the amount of change in the glacier in this study area will be determined by processing and comparing the measurements of 2 or more periods. The accuracy of the amount of volumetric change will be determined as specified in the study of Martín Español et al. (2016) using the depth model accuracy information obtained as a result of this study.

## 6. Acknowledgment

This study was funded by The Scientific and Technological Research Council of Türkiye (TÜBİTAK), 1071 program, project no: 121N033. This study was carried under the auspices of the Presidency of the Republic of Türkiye, supported by the Ministry of Industry and Technology, and coordinated by TÜBİTAK MAM Polar Research Institute.

## References

Bandini F, Kooij L, Mortensen BK, Caspersen MB, Thomsen LG et al. (2023a). Mapping inland water bathymetry with ground penetrating radar (GPR) on board unmanned aerial systems (UASs). Journal of Hydrology 616: 128789. https://doi.org/10.1016/j.jhydrol.2022.128789

Benedetto A, Tosti F, Ciampoli LB, D'amico F (2017). An overview of ground-penetrating radar signal processing techniques for road inspections. Signal Processing 132: 201-209. https://doi.org/10.1016/j.sigpro.2016.05.016

Benedetto F, Tosti F (2017). A signal processing methodology for assessing the performance of ASTM standard test methods for GPR systems. Signal Processing 132: 327-337. https://doi.org/10.1016/j.sigpro.2016.06.030

Bevington PR, Robinson DK, Blair JM, Mallinckrodt AJ, McKay S (1993). Data reduction and error analysis for the physical sciences. Computers in Physics 7 (4): 415-416. https://doi.org/10.1063/1.4823194

Bianchini Ciampoli L, Tosti F, Economou N, Benedetto F (2019). Signal processing of GPR data for road surveys. Geosciences 9 (2): 96. https://doi.org/10.3390/geosciences9020096

Blindow N, Salat C, Casassa G (2012). Airborne GPR sounding of deep temperate glaciers—Examples from the Northern Patagonian Icefield. In: 14th International Conference on Ground Penetrating Radar.

Campbell S, Affleck RT, Sinclair S (2018). Ground-penetrating radar studies of permafrost, periglacial, and near-surface geology at McMurdo Station, Antarctica. Cold Regions Science Technology 148: 38-49. https://doi.org/10.1016/j.coldregions.2017.12.008

Cheng Q, Su Q, Binley A, Liu J, Zhang Z et al. (2023). Estimation of surface soil moisture by a multi-elevation UAV-based ground penetrating radar. Water Resources Research 59 (2): e2022WR032621. https://doi.org/10.1029/2022WR032621

Church GJ, Bauder A, Grab M, Hellmann S, Maurer H (2018). High-resolution helicopter-borne ground penetrating radar survey to determine glacier base topography and the outlook of a proglacial lake. In: 17th International Conference on Ground Penetrating Radar.

Colorado J, Perez M, Mondragon I, Mendez D, Parra C et al. (2017). An integrated aerial system for landmine detection: SDR-based ground penetrating radar onboard an autonomous drone. Advanced Robotics 31 (15): 791-808. https://doi.org/10.1080/01691864.2017.1351393

Dix CH (1955). Seismic velocities from surface measurements. Geophysics 20 (1): 68-86. https://doi.org/10.1190/1.1438126

Economou N, Vafidis A, Benedetto F, Alani AM (2015). GPR data processing techniques. Civil Engineering Applications of Ground Penetrating Radar 281-297. https://doi.org/10.1007/978-3-319-04813-0

Egli PE, Irving J, Lane SN (2021). Characterization of subglacial marginal channels using 3-D analysis of high-density ground-penetrating radar data. Journal of Glaciology 67 (264): 759-772. https://doi.org/10.1017/jog.2021.26

Engel Z, Nývlt D, Láska K (2012). Ice thickness, areal and volumetric changes of Davies Dome and Whisky Glacier (James Ross Island, Antarctic Peninsula) in 1979–2006. Journal of Glaciology 58 (211): 904-914. https://doi.org/10.3189/2012JoG11J156

Fernández MG, López YÁ, Arboleya AA, Valdés BG, Vaqueiro YR et al. (2018). Synthetic aperture radar imaging system for landmine detection using a ground penetrating radar on board a unmanned aerial vehicle. IEEE Access 6: 45100-45112. https://doi.org/10.1109/ACCESS.2018.2863572

Forte E, Santin I, Ponti S, Colucci R, Gutgesell P et al. (2021). New insights in glaciers characterization by differential diagnosis integrating GPR and remote sensing techniques: a case study for the Eastern Gran Zebrù glacier (Central Alps). Remote Sensing of Environment 267: 112715. https://doi.org/10.1016/j.rse.2021.112715

Fu H, Liu Z, Guo X, Cui H (2018). Double-frequency ground penetrating radar for measurement of ice thickness and water depth in rivers and canals: development, verification and application. Cold Regions Science Technology 154: 85-94. https://doi.org/10.1016/j.coldregions.2018.06.017

Garcia Fernandez M, López YÁ, Andrés FLH. (2020). Airborne multi-channel ground penetrating radar for improvised explosive devices and landmine detection. IEEE Access 8: 165927-165943. :https://doi.org/10.1109/ACCESS.2020.3022624

Garcia Fernandez M, Alvarez Lopez Y, Las Heras F, Gonzalez Valdes B, Rodriguez Vaqueiro Y et al. (2018). GPR system onboard a UAV for non-invasive detection of buried objects. In: 2018 IEEE International Symposium on Antennas and Propagation and USNC/URSI National Radio Science Meeting.

Godio A, Rege RB (2015). The mechanical properties of snow and ice of an alpine glacier inferred by integrating seismic and GPR methods. Journal of Applied Geophysics 115: 92-99. https://doi.org/10.1016/j.jappgeo.2015.02.017

Grab M, Bauder A, Ammann F, Langhammer L, Hellmann S et al. (2018). Ice volume estimates of Swiss glaciers using helicopter-borne GPR—An example from the Glacier de la Plaine Morte. In: 17th International Conference on Ground Penetrating Radar.

Healy D, Katopodis C, Tarrant P (2007). Application of ground penetrating radar for river ice surveys. In: CGU HS Committee on River Ice Processes and the Environment, 14th Workshop on the Hydraulics of Ice Covered Rivers, Quebec City.

Ivins ER, James TS (2005). Antarctic glacial isostatic adjustment: a new assessment. Antarctic Science 17 (4): 541-553. https://doi.org/10.1017/S0954102005002968

Jenssen ROR, Jacobsen SK (2021). Measurement of snow water equivalent using drone-mounted ultra-wide-band radar. Remote Sensing 13 (13): 2610. https://doi.org/10.3390/rs13132610

Jol HM (2008). Ground penetrating radar theory and applications: Elsevier.

Lamsters K, Karušs J, Krievāns M, Ješkins J (2020). High-resolution surface and BED topography mapping of Russell Glacier (SW Greenland) using UAV and GPR. 2: 757-763.

Lapazaran J, Otero J, Martín Español A, Navarro F (2016a). On the errors involved in ice-thickness estimates II: errors in digital elevation models of ice thickness. Journal of Glaciology 62 (236): 1021-1029. http://doi.org/10.1017/jog.2016.94

Lapazaran J, Otero J, Martín Español A, Navarro F (2016b). On the errors involved in ice-thickness estimates I: ground-penetrating radar measurement errors. Journal of Glaciology 62 (236): 1008-1020. https://doi.org/10.1017/jog.2016.93

Machguth H, Eisen O, Paul F, Hoelzle M (2006). Strong spatial variability of snow accumulation observed with helicopter-borne GPR on two adjacent Alpine glaciers. Geophysical Research Letters 33 (13). https://doi.org/10.1029/2006GL026576

Martín Español A, Lapazaran J, Otero J, Navarro F. (2016). On the errors involved in ice-thickness estimates III: error in volume. Journal of Glaciology 62 (236): 1030-1036. https://doi.org/10.1017/jog.2016.95

Merz K, Maurer H, Buchli T, Horstmeyer H, Green AG et al. (2015). Evaluation of ground-based and helicopter ground-penetrating radar data acquired across an Alpine rock glacier. Permafrost Periglacial Processes 26 (1): 13-27. https://doi.org/10.1002/ppp.1836

Mingo L, Flowers GE (2010). An integrated lightweight ice-penetrating radar system. Journal of Glaciology 56 (198): 709-714. https://doi.org/10.3189/002214310793146179

Mueller T, Pusuluri N, Mathias K, Cornelius P, Barnhisel R et al. (2004). Map quality for ordinary kriging and inverse distance weighted interpolation. Soil Science Society of America Journal 68 (6): 2042-2047. :https://doi.org/10.2136/sssaj2004.2042

Navarro F, Martín Español A, Lapazaran J, Grabiec M, Otero J et al. (2014). Ice volume estimates from ground-penetrating radar surveys, Wedel Jarlsberg Land glaciers, Svalbard. 46 (2): 394-406.

Negi H, Snehmani NT, Sharma J (2008). Estimation of snow depth and detection of buried objects using airborne ground penetrating radar in Indian Himalaya. Current Science 865-870.

Oliva M, Navarro F, Hrbáček F, Hernandéz A, Nývlt D et al. (2017). Recent regional climate cooling on the Antarctic Peninsula and associated impacts on the cryosphere. Science of the Total Environment 580: 210-223. https://doi.org/10.1016/j.scitotenv.2016.12.030

Richards E, Stuefer S, Rangel RC, Maio C, Belz N et al. (2023). An evaluation of GPR monitoring methods on varying river ice conditions: a case study in Alaska. Cold Regions Science Technology 210: 103819. https://doi.org/10.1016/j.coldregions.2023.103819

Rignot E, Vaughan DG, Schmeltz M, Dupont T, MacAyeal D (2002). Acceleration of Pine island and Thwaites glaciers, West Antarctica. Annals of Glaciology 34: 189-194. https://doi.org/10.3189/172756402781817950

Rippa S (1999). An algorithm for selecting a good value for the parameter c in radial basis function interpolation. Advances in Computational Mathematics 11 (2): 193-210. https://doi.org/10.1023/A:1018975909870

Ruols B, Baron L, Irving J (2022). Drone-based GPR system for 4D glacier data acquisition. In: EGU General Assembly Conference Abstracts.

Rutishauser A, Maurer H, Bauder A (2016). Helicopter-borne ground-penetrating radar investigations on temperate alpine glaciers: a comparison of different systems and their abilities for bedrock mapping. Geophysics 81 (1): WA119-WA129. https://doi.org/10.1190/geo2015-0144.1

Rückamp M, Braun M, Suckro S, Blindow N (2011). Observed glacial changes on the King George Island ice cap, Antarctica, in the last decade. Global and Planetary Change 79 (1-2): 99-109. https://doi.org/10.1016/j.gloplacha.2011.06.009

Saponaro A, Dipierro G, Cannella E, Panarese A, Galiano AM et al. (2021). A UAV-GPR fusion approach for the characterization of a quarry excavation area in Falconara Albanese, Southern Italy. Drones 5 (2): 40. https://doi.org/10.3390/drones5020040

Selbesoğlu MO, Bakirman T, Vassilev O, Ozsoy B (2023). Mapping of glaciers on Horseshoe Island, Antarctic Peninsula, with deep learning based on high-resolution orthophoto. Drones 7 (2): 72. https://doi.org/10.3390/drones7020072

Shanock LR, Baran BE, Gentry WA, Pattison SC, Heggestad ED (2010). Polynomial regression with response surface analysis: A powerful approach for examining moderation and overcoming limitations of difference scores. Journal of Business and Psychology 25 (4): 543-554. https://doi.org/10.1007/s10869-013-9317-6

Sibson R (1981). A brief description of natural neighbour interpolation. Interpreting Multivariate Data 21-36.

Steinbeck L, Mester A, Zimmermann E, Klotzsche A, van Waasen S (2022). In situ time-zero correction for a ground penetrating radar monitoring system with 3000 antennas. Measurement Science Technology 33 (7): 075904. https://doi.org/10.1088/1361-6501/ac632b

Taurisano A, Tronstad S, Brandt O, Kohler J (2006). On the use of ground penetrating radar for detecting and reducing crevasse-hazard in Dronning Maud Land, Antarctica. Cold Regions Science Technology 45 (3): 166-177. https://doi.org/10.1016/j.coldregions.2006.03.005

Thompson LG (2000). Ice core evidence for climate change in the Tropics: implications for our future. Quaternary Science Reviews 19 (1-5): 19-35. https://doi.org/10.1016/S0277-3791(99)00052-9

Turner J, Barrand NE, Bracegirdle TJ, Convey P, Hodgson DA et al. (2014). Antarctic climate change and the environment: an update. Polar Record 50 (3): 237-259. https://doi.org/10.1017/S0032247413000296

Vergnano A, Franco D, Godio A (2022). Drone-borne ground-penetrating radar for snow cover mapping. Remote Sensing 14 (7): 1763. https://doi.org/10.3390/rs14071763

Wu K, Lambot S (2022a). Digital soil mapping using drone-borne ground-penetrating radar. In: Instrumentation and Measurement Technologies for Water Cycle Management (pp. 417-436): Springer. https://doi.org/10.1109/TGRS.2022.3198431

Wu K, Lambot S (2022b). Analysis of low-frequency drone-borne GPR for root-zone soil electrical conductivity characterization. IEEE Transactions on Geoscience Remote Sensing 60: 1-13.

Wu K, Rodriguez GA, Zajc M, Jacquemin E, Clément M et al. (2019). A new drone-borne GPR for soil moisture mapping. Remote Sensing of Environment 235: 111456. https://doi.org/10.1016/j.rse.2019.111456

Yilmaz Ö (2001). Seismic data analysis: Processing, inversion, and interpretation of seismic data: Society of exploration geophysicists.